

## Research Article

# Green Synthesis of S- and N-Codoped Carbon Nanospheres and Application as Adsorbent of Pb (II) from Aqueous Solution

Nadia Hussain,<sup>1</sup> Salam Alwan ,<sup>2</sup> Hassan Alshamsi,<sup>3</sup> and Ibrahim Sahib<sup>4</sup>

<sup>1</sup>College of Biotechnology, University of Al-Qadisiyah, Diwaniya, Iraq

<sup>2</sup>College of Dentistry, University of Al-Qadisiyah, Diwaniya, Iraq

<sup>3</sup>Department of Chemistry, College of Education, University of Al-Qadisiyah, Diwaniya, Iraq

<sup>4</sup>College of Dentistry, Alkafeel University, Najaf, Iraq

Correspondence should be addressed to Salam Alwan; [salamhussein354@gmail.com](mailto:salamhussein354@gmail.com)

Received 9 July 2019; Revised 11 September 2019; Accepted 8 October 2019; Published 16 March 2020

Academic Editor: Maurizio Volpe

Copyright © 2020 Nadia Hussain et al. This is an open access article distributed under the Creative Commons Attribution License, which permits unrestricted use, distribution, and reproduction in any medium, provided the original work is properly cited.

In this paper, green and facile synthesis of sulfur- and nitrogen-codoped carbon nanospheres (CNs) was prepared from the extract of *Hibiscus sabdariffa* L by a direct hydrothermal method. Finally, sulfur-carbon nanospheres (CNs) were used as the adsorbent to remove Pb<sup>+2</sup> ions from aqueous solutions because of the high surface area of S-CN from CNs and N-CN. The synthesized nanospheres were examined by Fourier transform infrared (FTIR) spectroscopy, X-ray diffraction (XRD), field emission scanning electron microscopy, transmission electron microscopy (TEM), and nitrogen adsorption-desorption isotherms. The results show spherical shapes have a particle size of up to 65 nm with a high surface area capable of absorbing lead ions efficiently. Additionally, the factors affecting the process of adsorption that include equilibrium time, temperature, pH solution, ionic intensity, and adsorbent dose were studied. The equilibrium removal efficiency was studied employing Langmuir, Freundlich, and Temkin isotherm forms. The kinetic data were analyzed with two different kinetic models, and both apply to the adsorption process depending on the values of correlation coefficients. The thermodynamic parameters including Gibbs free energy ( $\Delta G^\circ$ ), standard enthalpy change ( $\Delta H^\circ$ ), and standard entropy change ( $\Delta S^\circ$ ) were calculated for the adsorption process.

## 1. Introduction

After discovering various forms of carbon, for instance, fullerenes and carbon nanotubes, researchers went on to use the carbon material in a broader form [1]. Including these nanodesigned carbon substances, the carbon nanospheres have drawn large considerations owing to their various uses in catalyst supports, anodes for lithium-ion batteries, electrodes for supercapacitors, lubricants, polymer, and rubber additives, which result from their exceptional properties, for instance, superior chemical stability, thermal insulation, low density, and high compressive strength [2–8]. There are many different methods to synthesis the carbon nanospheres involving arc plasma technique [9], catalyzed pyrolysis [10], self-generated template manner [11], hydrothermal reaction [12], spray pyrolysis [13] and chemical vapor deposition (CVD) [14], etc. Currently, friendly environment synthesis

technique has been advanced including transformation of easily obtainable precursors, for example, glucose [15] and cyclodextrins to carbon nanospheres beneath moderate conditions (hydrothermal reaction at 160–180°C) [16]. This preparation method is clear as it does not use organic solvents and poisonous reagents. The surface of the resulting CNs contains rich hydrophilic functional groups, for example, C-OH, C-O, and C-OOH. There has been just a little research on an investigation of CNs in water remediation due to the presence of oxygen functional groups [17]. The carbon nanospheres could present good adsorption efficiency towards heavy metals. For activated carbon and different kinds of carbon nanomaterials, there has been exceedingly preparation to increase that the adsorption capacities for the sake of heavy metals can be reinforced by chemical remediation with acids and bases [18, 19]. This hydrothermal synthesis method has numerous benefits, for instance, modest temperatures,

effective produces, and modest temperatures, good produce, and ultimate importantly a friendly environmentally operation, a “green” technique. Nevertheless, the study of the development procedure of CNs manufactured by hydrothermal methods is comparatively elusive. The major problem in conception of this mechanism is that the reaction takes place in a closed inaccessible vessel, and some experiments have been made to study the hydrothermal reaction in situ using Raman spectroscopy, but further performance is necessary to gain a conception of the growth process [20]. Several methods have been used for the removal of heavy metals from wastewater, involving physical, chemical, and biological methods. Nevertheless, the greatest, suitable, and effective procedure for the removal of heavy metals from aqueous environment is the adsorption process [21].

In the current work, the carbon spheres, sulfur- and nitrogen-doped carbon nanospheres, were prepared by hydrothermal technique and from the green material *Hibiscus sabdariffa* L extract. And finally we used sulfur-carbon as the surface to remove  $\text{Pd}^{+2}$  ion from the contaminated water. Batch studies were performed by varying the contact time, temperature, pH solution, and ionic intensity, where the size of the samples prepared and the morphology were identified using the characterization techniques mentioned.

## 2. Experimental Section

**2.1. Chemicals.** Sulphuric acid, sodium hydroxide, and HCl, which were bought from Scharlau, were used directly without primary purification. Each solution was prepared utilizing deionized water.

**2.2. Characterization.** The crystalline property of the samples can be identified using X-ray technology with a wavelength of 1.54056 Å in the range of from 5° to 80° and with a scanning velocity of up to 0.03 s<sup>-1</sup>. The functional groups of the compounds are shown as bands by FT-IR analysis in the range 4000–400 cm<sup>-1</sup> with KBr tablets as substance holders. The Brunauer-Emmett-Teller (BET) surface areas were measured from the N<sub>2</sub> adsorption using a Quadrasorb SIMP. The outer shape of the nanoparticles prepared can be identified by the field emission scanning electron microscopy and quickening voltage up to 8.0 kV, as well as transmission electron microscopy and quickening voltage up to 200 kV. Thermal gravimetric analysis (TGA) and a high-temperature thermal analyzer were used to identify the thermal stability of prepared materials with a heating speed of up to 10°C·min<sup>-1</sup> in range (50–600)°C using Arcon gas. The mechanical properties and the three-dimensional shape of the sample surface were obtained from atomic force microscopy (AFM) of the Park Systems XE-70.

**2.3. Preparation of *Hibiscus sabdariffa* L Extract.** 10 g of plant sepal powder was added to 50 ml of deionized water with heating and stirring on a magnetic stirrer hot plate for 30 min till the temperature of boiling was achieved. Then, the mixture was filtered and the filtrate was cooled to room

temperature. Furthermore, the mixture was diluted to 100 ml with deionized water to achieve 10 % extract solution.

**2.4. Synthesis of the Carbon Nanospheres, Sulfur- and Nitrogen-Doped Carbon Nanospheres Using *Hibiscus sabdariffa* L Extract.** The carbon spheres, sulfur- and nitrogen-doped carbon nanospheres, were synthesized via the one-pot hydrothermal method. CNs were synthesized using *Hibiscus sabdariffa* L extract as a carbon source. In an ideal experiment, 50 mL of extract was put in a 100 mL teflon-lined stainless steel autoclave. The autoclave was closed cautiously and heated to 180°C for 5 hours in an oven. Through this method, a liquid different from red to sable black was obtained, which confirmed the formation of CNs. Then, the liquid was spontaneously cooled to room temperature and centrifuged at 10000 rpm for 15 min to eliminate the greater or conglomerate atoms. The suspension was collected and dried employing an oven for abstraction of water. The produced solid substance was saved for the other purpose. Pure sulfur- and nitrogen-doped carbon nanospheres were obtained via a similar process, but 2 mL of NH<sub>3(aq)</sub> solution was added in extract to prepare N-CNs and 1 mL of concentrated sulfuric acid (98%) was added in extract to prepare S-CNs [22, 23] Table 1.

**2.5. The Study of Adsorption of  $\text{Pd}^{+2}$ .** Prepare a set of lead ion solutions in the range (1–20 ppm) to the prepared three surfaces (0.2 g of S- and N-co-doped carbon nanospheres) to determine the best surface giving high adsorption efficiency. All solutions are stirred using a shaker water bath for 60 min at a speed of up to 150 rpm. After the adsorption reaction is finished, separate all the solutions using the centrifuge for 10 min with a speed of up to 3000 rpm. Then, measure the absorbance (A) of all solutions using an atomic absorption spectrophotometer. Finally, calculate the amount of material absorbed ( $q_e$ ) by the following equation [24]:

$$q_e = \frac{V_{\text{sol}}(C_o - C_e)}{m} \quad (1)$$

$$\text{Removal \%} = \frac{(C_o - C_e)}{C_o} * 100,$$

where  $q_e$  (mg/g) is the quantity of adsorbent material,  $m$  (g) is the weight of surface,  $V$  (L) is the volume of mixture,  $C_o$  (mg/L) is the original concentration, and  $C_e$  (mg/L) is the equilibrium concentration, while the other factors affecting the adsorption process are studied in the same way, for instance, pH, ionic intensity, time, and temperature.

## 3. Results and Discussion

### 3.1. Characterization

**3.1.1. FTIR Analysis.** The functional groups of the prepared nanospheres were detected by Fourier transform infrared (FTIR). Figure 1 shows the FTIR spectrum of carbon nanospheres and its derivatives. The hydroxyl peak of CNs shows in the stretch (3300–3540 cm<sup>-1</sup>). The

TABLE 1: List of some previous work prepared of CNs.

Materials	Synthesis method	Conditions	Applications	Ref.
NMCNs	The facile organic-organic self-assembly	Ethanol (10 mL), H <sub>2</sub> O (40 ML), stirring for 25 min, 0.1 mL of EDA and 0.26 g of phloroglucinol, 0.26 g of HMT	Acid red 57 molecules adsorption	[37]
CNs	Hydrothermal method	4 g C <sub>6</sub> H <sub>12</sub> O <sub>6</sub> ·H <sub>2</sub> O and 40 mL water at 180°C for 6 h, vacuum dried at 80°C for 12 h.	Removal of organic dyes	[38]
Fe/N-C	In situ carbothermal reduction synthesis	1.0 g of dopamine, 1.76 mmol of FeCl <sub>3</sub> ·6H <sub>2</sub> O, 10 min, 10 mmol of tris, stirred for 30 h	U (VI) adsorption and reduction	[39]
NMCNs	The facile organic-organic self-assembly			
Fe-NMCNs	Hexamine-induced coassembly route	0.4 g of F127, 5 mL of HC, 0.2 g of 3-aminophenol, 43 mL water/ethanol (35:8, v/v), 1 h, 0.1 g of hexamine	Acid red 57 (AR) and basic fuchsin (BF) adsorption	[40]

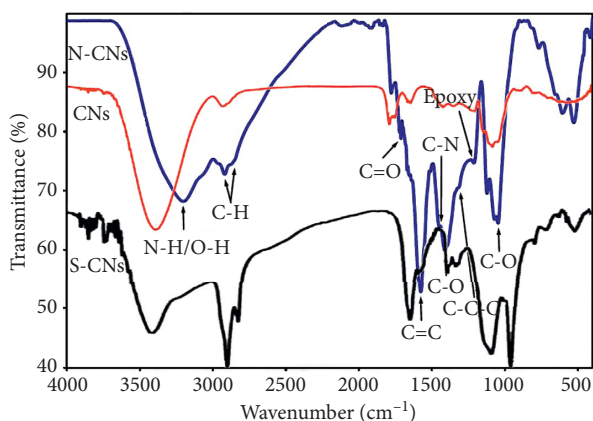


FIGURE 1: FTIR analysis of CNs, N-CNs, and S-CNs.

carbonyl peak appears in the stretch ( $1710\text{ cm}^{-1}$ ), and the C=C peak appears in the stretch ( $1648\text{ cm}^{-1}$ ). Finally, two peaks at  $1190$  and  $1036\text{ cm}^{-1}$  attributed to the stretch to C-O and C-O-C bonds, respectively [25]. The FT-IR spectrum of N-CNs shows distinctive absorption peaks of hydroxyl and amine appear stretch at  $3257\text{ cm}^{-1}$  and peak at  $2919\text{ cm}^{-1}$  assigned to C-H group. The bands appearing at  $1299$ ,  $1105$ , and  $1027\text{ cm}^{-1}$  demonstrate carboxyl groups [25, 26].

The FT-IR analysis of S-CNs exhibits the band on stretch at  $1038\text{ cm}^{-1}$  is attributed to C-O, S-O, and C-O-C bonds, while the C-O and C-S bonds appear on stretch at  $1194\text{ cm}^{-1}$  and COO<sup>-</sup> groups appear between  $1396$ – $1496\text{ cm}^{-1}$ . The bands appear at  $1638$ ,  $2643$ , and  $2928\text{ cm}^{-1}$  attributed to C=O, S-H, and C-H bonds. Finally, the wide band at  $3246$ – $3595\text{ cm}^{-1}$  attributed to the hydroxyl bond [27, 28].

**3.1.2. XRD Analysis.** The phase structure and degree of crystallinity of prepared nanospheres were determined by XRD. Figure 2 shows the XRD pattern of the CNs, N-CNs, and S-CNs. The pattern of CNs shows an intense XRD peak broad in range ( $2\theta = 19$ – $21^\circ$ ), which applies on d-spacing of ( $4.50$ ,  $4.34$ , and  $4.08$ ) Å, while the XRD pattern of S-CNs appear a wide diffraction band at  $23.6^\circ$  that applies on d-spacing of  $5.48$  Å, where the presence of functional groups on the surface of S-CNs makes it larger interlayer

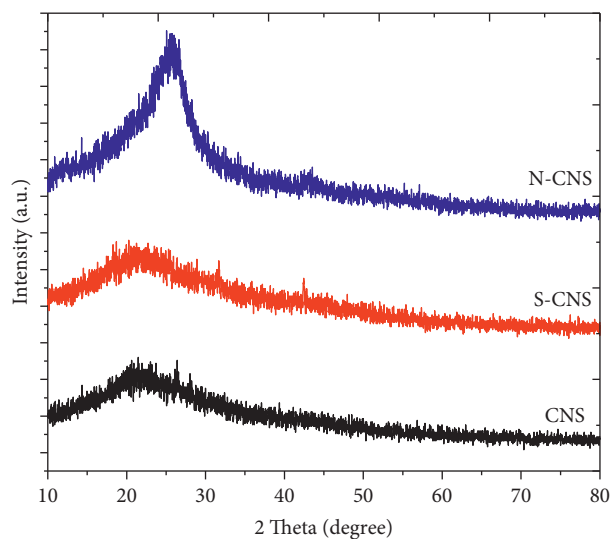


FIGURE 2: XRD pattern of CNs, S-CNs, and N-CNs.

spacing than of CNs. Also, the presence of ammonia groups on the N-CNs surface makes it a more sharp peak than CNs [23, 29].

**3.1.3. FE-SEM Images of Nanospheres.** The surface morphology of the carbon nanospheres was noticed employing FE-SEM analysis. Figure 3 shows balls of different sizes with similar morphology and are composed of blocks with a uniform homogeneity and good connectivity between the balls. The sphere sizes of the CNs, N-CNs, and S-CNs are almost  $2\text{ }\mu\text{m}$  [28].

**3.1.4. TEM Images of Nanospheres.** TEM technique provides information about the external surface of prepared nanomaterials. The technique works by passing a beam of electrons during the material to give the picture of FE-SEM [30]. Figure 4 shows TEM image of CNs, N-CNs and S-CNs multiple conglomerates of the carbon spheres are abundant and, in some cases, chains of beads-like accretions of the carbon spheres. No obvious spherical assemblies are found in the TEM image of the S-CNs, which is indicative of their amorphous nature [23].

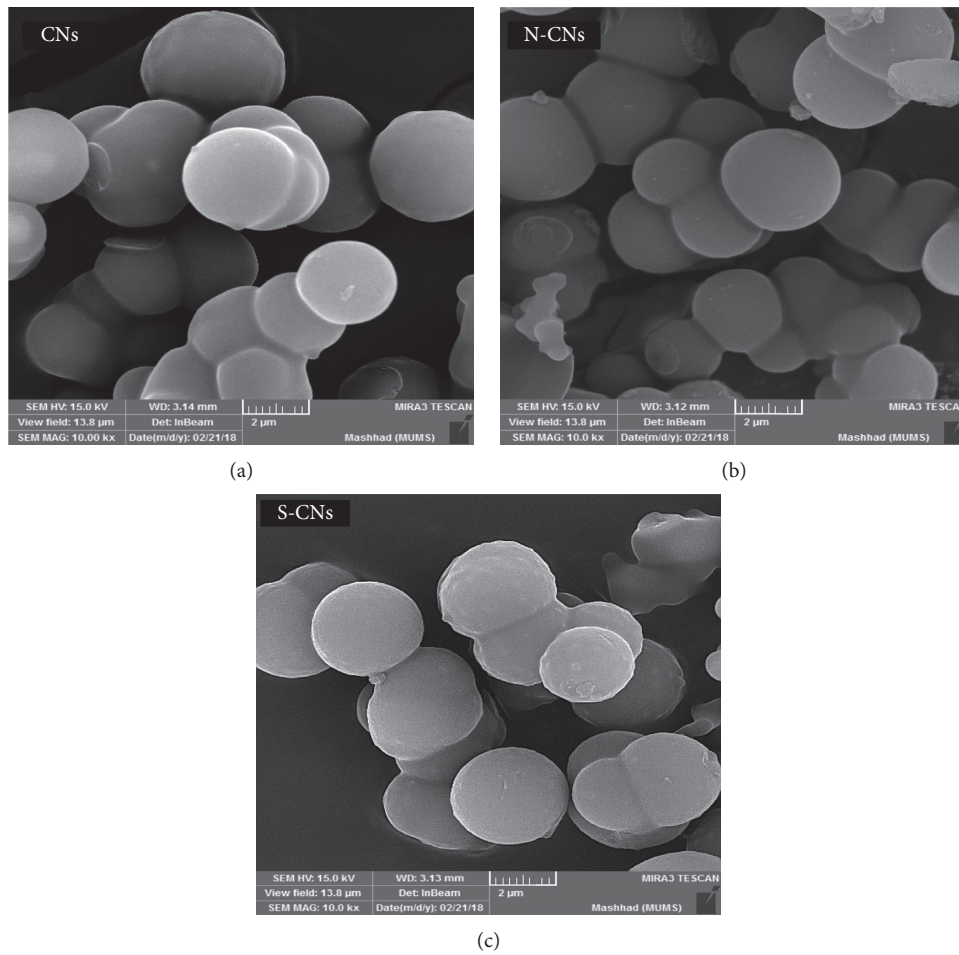


FIGURE 3: FE-SEM images of (a) CNs, (b) N-CNs, and (c) S-CNs.

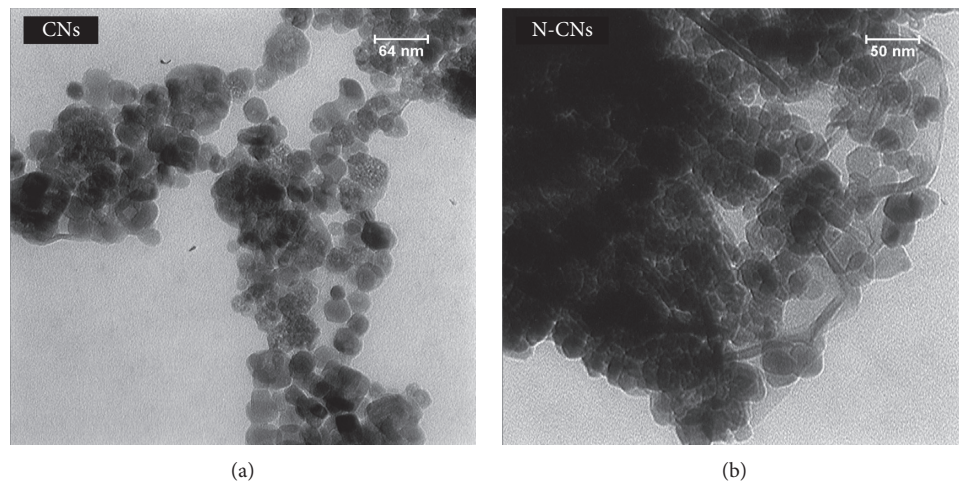
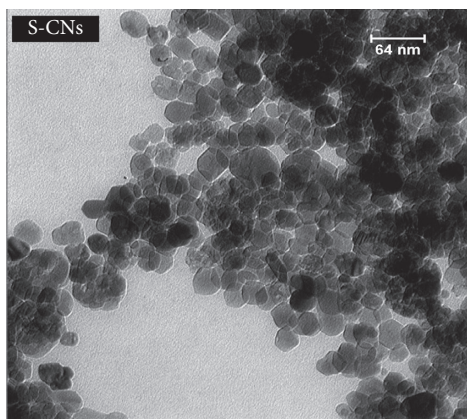


FIGURE 4: Continued.



(c)

FIGURE 4: TEM images of (a) CNs, (b) N-CNs, and (c) S-CNs.

**3.1.5. BET Analysis.** The specific surface area is estimated by using the Brunauer-Emmett-Teller (BET) manner, and the pore size distributions are found by means of the Barrett-Joyner-Halenda (BJH) method equation using the adsorption isotherm model, which are shown in Figure 5. The surface area (BET) and the pore diameter of carbon nanospheres (CNs) were obtained to be  $122.2 \text{ m}^2/\text{g}$  and  $22.55 \text{ nm}$ , respectively. The value of the pore diameter suggested that CNs were a mesoporous material. The isotherm displays a typical type-III shaped curve and no hysteresis loop, while the N-CNs were found to be  $179.1 \text{ m}^2/\text{g}$  and  $8.78 \text{ nm}$ , respectively. The isotherm exhibits a typical type-IV shaped curve and a H2 present hysteresis loop, pointing out the presence of slit-shaped pores between the parallel layers of nanospheres. Finally, the S-CNs have the surface area up to  $196.3 \text{ m}^2/\text{g}$  and pore diameter  $12.41 \text{ nm}$ . Figure 5 exhibits a typical type-V shaped curve and a H1 present hysteresis loop, and this isotherm is convex to the relative pressure axis and is the characteristic of weak adsorbate-adsorbent interactions. Hysteresis loop H1 refers to porous materials which consist of well-aligned spheres and briquettes, and materials of this type tend to have relatively narrow distributions of pore size [21, 31].

**3.1.6. TGA Analysis.** TGA is a technique that gives information on the thermal stability of the prepared carbon nanospheres and is exhibited in Figure 6, when  $100^\circ\text{C}$  weight loss of 4% is due to the subtraction of water molecules, in the range of  $100^\circ\text{C}$  to  $200^\circ\text{C}$  weight loss of 6%. Finally, when the temperature increases to  $435^\circ\text{C}$ , the weight loss of 90% is owing to the gradual removal of functional groups on the surface of CNs, while the TGA curve of N-CNs shows two stages of weight loss: *first stage* of weight loss of 70.2% in range from  $100^\circ\text{C}$  to  $350^\circ\text{C}$  as a result of removal of water from the sample with oxidation of the functional groups and their transformation into volatile gases, while the *second stage* weight loss is 28.9% in the range from  $350^\circ\text{C}$  to  $593.1^\circ\text{C}$  due to thermal decomposition of the remaining groups with carbon oxidation. Finally, in the TGA curve of S-CNs, all weight

losses become less compared with N-CNs. The mass loss was 58.7% at  $200\text{--}380^\circ\text{C}$ , owing to the elimination of water molecules, sulfur, and oxygen functional groups, while mass loss was about 40.8% in the range  $380\text{--}600^\circ\text{C}$ , owing to thermal decomposition of the functional groups of the S-CNs. A TGA analysis of the above samples shows that the thermal stability of S-CNs is higher than those of N-CNs [32].

**3.1.7. AEM Images of Nanospheres.** AFM is a technique that gives information on the thickness and morphology of the prepared carbon nanospheres. The AFM image in Figure 7 clearly indicates the presence of nanospheres. The average diameter of carbon nanospheres is  $4 \text{ nm}$  that due to the presence of oxygen-containing groups that increase the diameter of the substance. The average diameter of N-CNs is up to  $2.39 \text{ nm}$  (Table 2) owing to the removal of the remaining oxygen groups. Finally, the AFM image of the S-CN sample shows heterogeneous aggregated balls with an average diameter of up to  $2.87 \text{ nm}$ .

## 3.2. Adsorption Experiments

**3.2.1. Effect of Adsorbent Dosage.** An adsorption experiment of Pb (II) removal is performed using different weights ( $0.005\text{--}0.25 \text{ g}$ ) of the S-CNs. It was noticed that the lead ion removal percentage increased with increasing the weight of the nanospheres. This can be attributed to the greater surface area of S-CNs and the increase in the available active sites for metal ion adsorption. Consequently, the uptake of metal ion reaches a saturation level at  $0.2 \text{ g}$  nanospheres as the active sites present on the surface of S-CNs become saturated with Pb (II). For subsequent experiments,  $0.2 \text{ g}$  of sorbent dose was selected (Figure 8).

**3.2.2. Effect of Contact Time and Kinetics of Adsorption.** Lead ion adsorption has been studied at different times after ( $1\text{--}120 \text{ min}$ ). In Pb (II), adsorption capacity was increased with increasing the time to its maximum value (saturation

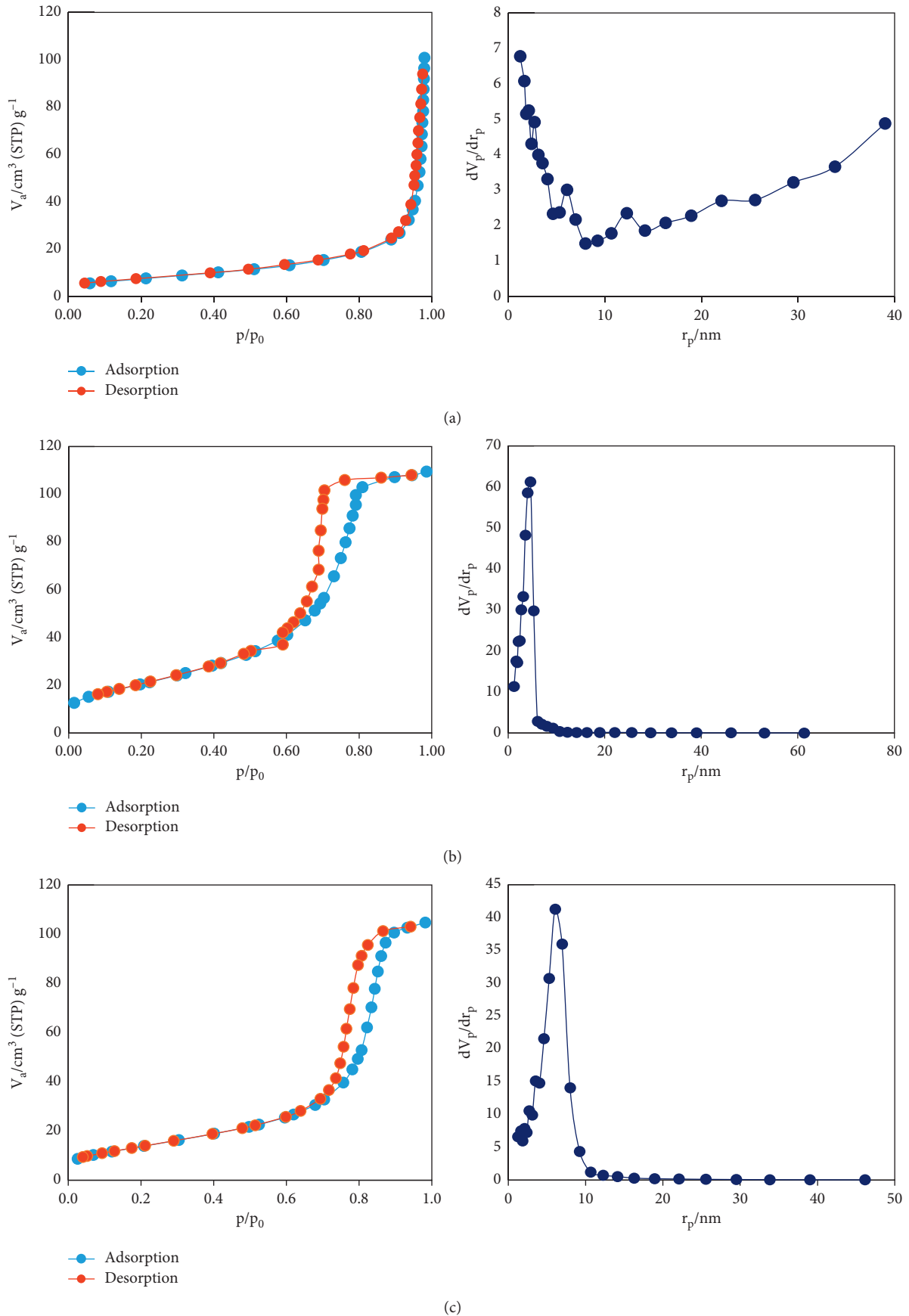


FIGURE 5: N<sub>2</sub> adsorption and desorption curves and pore size distributions of (a) CNs, (b) N-CN, and (c) S-CN.

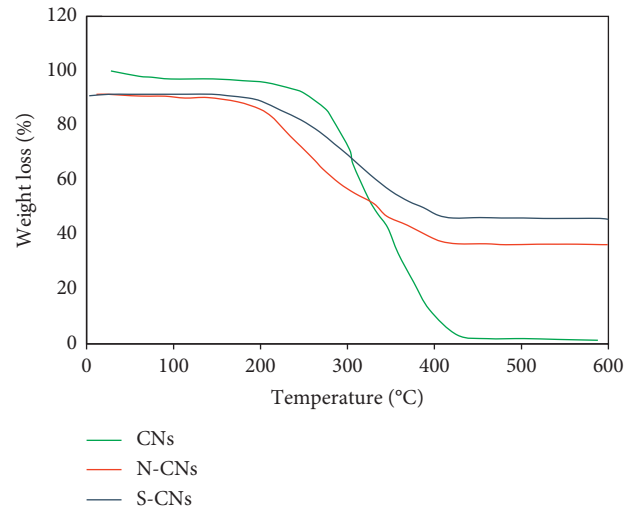


FIGURE 6: TGA analysis of CNs, N-CNs, and S-CNs.

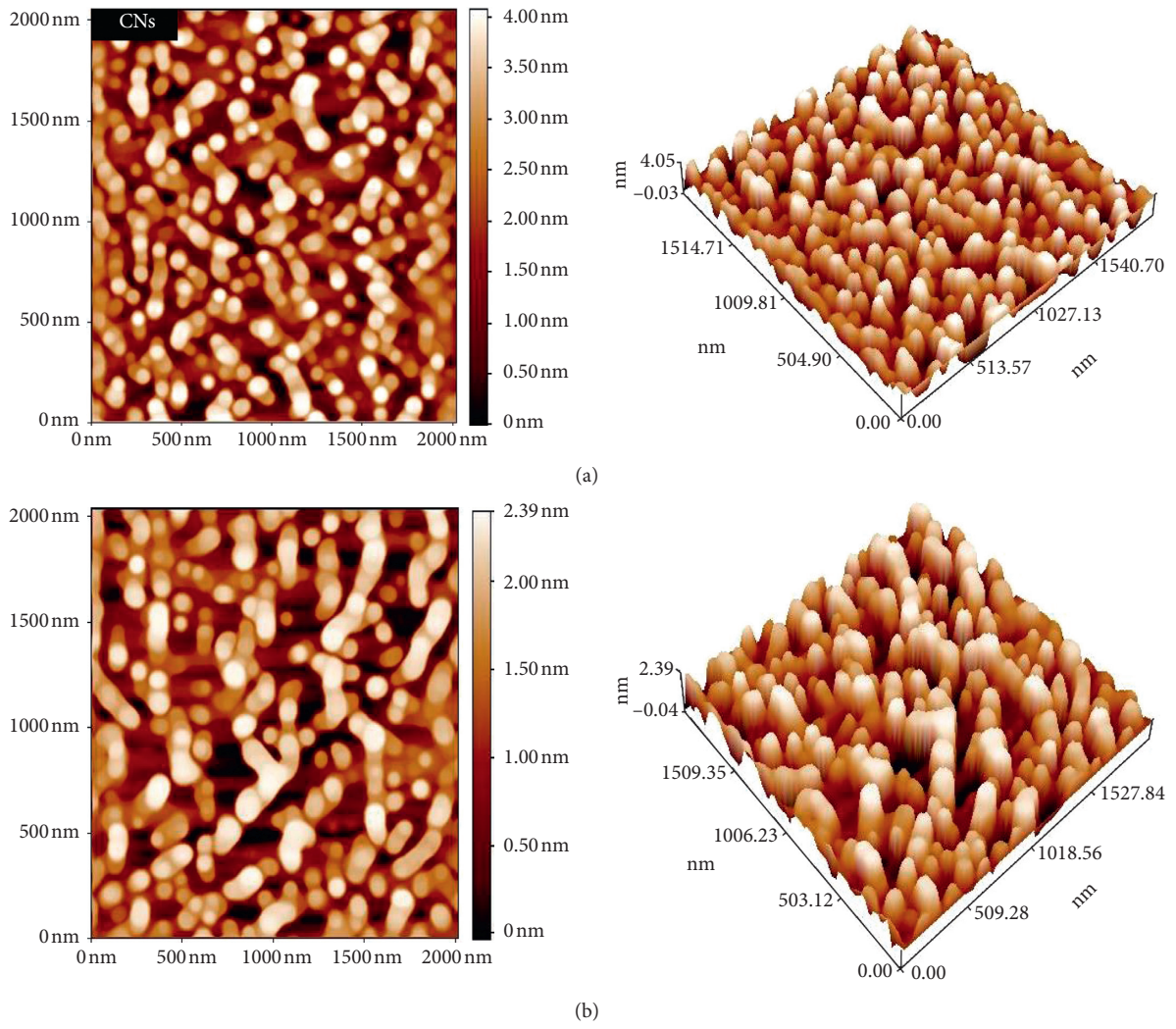


FIGURE 7: Continued.

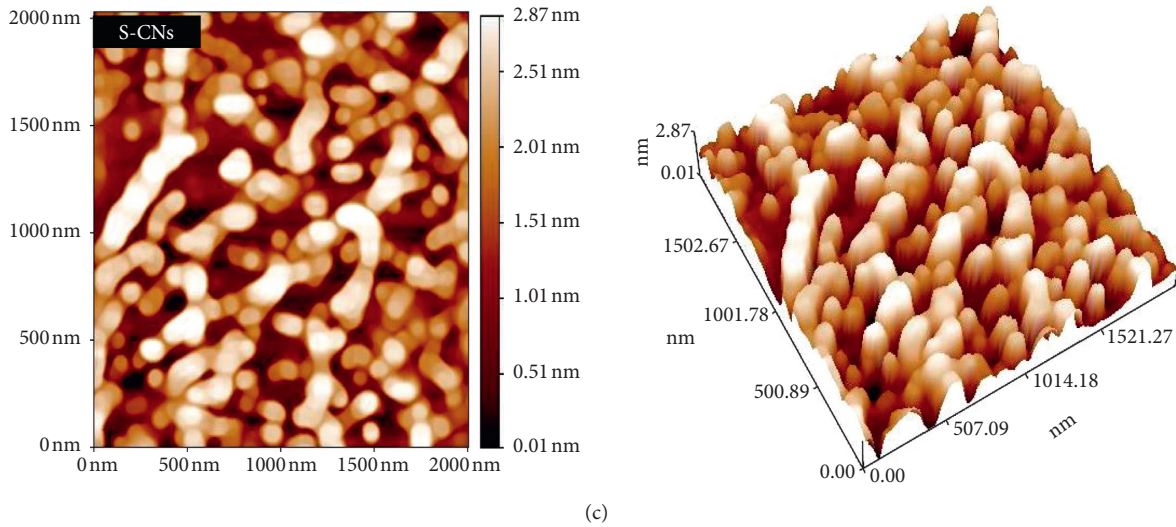


FIGURE 7: 2D and 3D images of (a) CNs, (b) N-CNs, and (c) S-CNs.

TABLE 2: The statistical roughness coefficients of prepared samples.

Amplitude factors	CNs	N-CNs	S-CNs
$R_a$ (nm)	0.9	0.55	0.65
$R_q$	1.06	0.65	0.76
$R_{sk}$	-0.14	-0.33	-0.26
$R_{ku}$	1.99	2.01	1.9
Thickness (nm)	4.00	2.39	2.87

state), but sometimes the adsorption capacity decreases with increasing time due to a desorption process (Figure 9).

In order to investigate the mechanism of adsorption and potential rate controlling steps, two kinetic models, namely, pseudo-first-order and pseudo-second-order equation models were analyzed. The pseudo-first-order equation is expressed as follows:

$$\log(q_e - q_t) = \log q_e - \frac{k_1}{2.303} t. \quad (2)$$

The equation above shows that  $k_1$  is the first-order velocity constant (1/min), where the drawing  $\log(q_e - q_t)$  with time gives a straight line. Through this, we obtain the amount of absorbent material and the first-order velocity constant of the intercept and slope, respectively, while the equation below describes the pseudo-second-order model:

$$\frac{t}{q_t} = \frac{1}{k_2 q_e^2} + \left(\frac{1}{q_e}\right) t, \quad (3)$$

where drawing  $t/q_t$  with time gives a linear relationship, from which we obtain the amount of the absorbent material and the second-order velocity constant (g/mg min) from the intercept and slope (Figure 10).

The kinetic parameters of all models and the correlation coefficients are shown in Table 3. The results show that the lead ion adsorption process on the surface of S-CNs is applied to the pseudo-second-order model because the value of  $R^2$  is equal to 1. The high  $R^2$  value is obtained for the pseudo-first-order model, indicating that the experimental data are well described by the pseudo-first-order model.

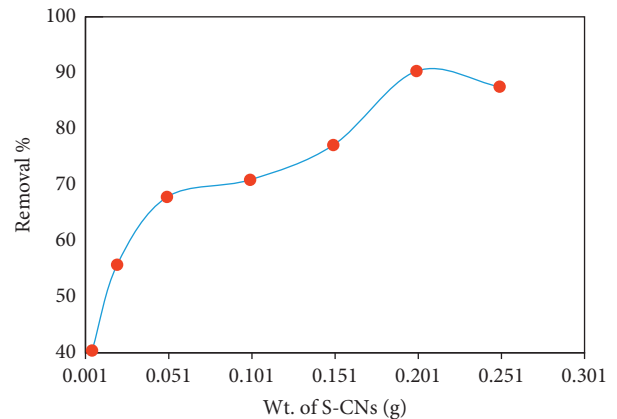


FIGURE 8: Effect of adsorbent dose on the removal percentage of Pb (II).

**3.2.3. Influence of the Acidic Function (pH).** The most important factor affecting lead ion adsorption is the acidic function due to the change in surface charge of the adsorbent material. The influence of the solution pH on Pb (II) removal by the S-CNs is displayed in Figure 11, where we notice that the rate of removal of Pb (II) on the surface of S-CNs increases with the increase of acid function. Because the lead ion has a positive charge at pH = 2, it decreases adsorption efficiency of the small hydrogen ions which have the ability to cover the lead ions as they are associated with the surface of S-CNs. However, increasing the value of pH = 12 increases the negative charges and increases the surface ability to absorb the lead ion very efficiently.

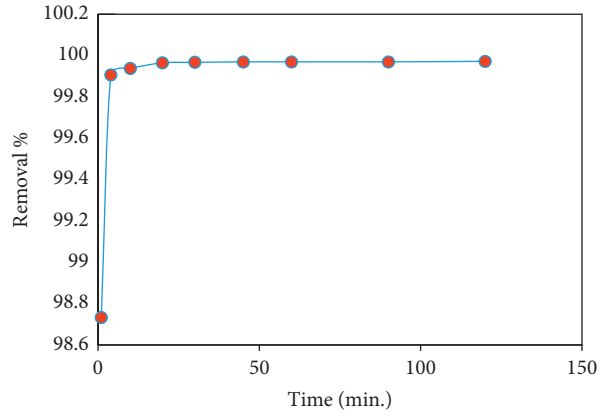


FIGURE 9: Effect of time equilibrium on the removal percentage of Pb (II).

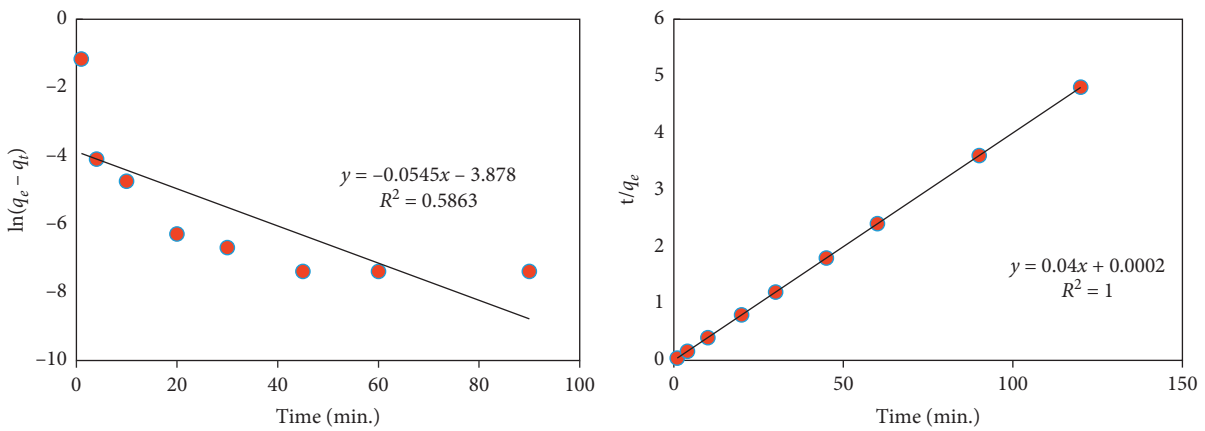


FIGURE 10: Pseudo-first- and Pseudo-second-order kinetics for adsorption of Pb (II). (a) 1st order and (b) 2nd order.

TABLE 3: Kinetics parameters of adsorption of Pb (II).

Metal	Pseudo first order			Pseudo second order			
	$k_1$	$q_e$	$R^2$	$k_2$	$q_e$	$h$	$R^2$
Pb (II)	0.086	2.298	0.921	0.191	23.809	108.690	1.000

3.2.4. *Adsorption Isotherm Models.* Three classic adsorption models, Langmuir, Freundlich, and Temkin, were used to describe the adsorption equilibrium. The mathematical representations of the Langmuir, Freundlich, and Temkin models are given below:

$$\frac{C_e}{q_e} = \frac{C_e}{q_m} + \frac{1}{K_L q_m},$$

$$\log q_e = \log K_f + \frac{1}{n} \log C_e, \tag{4}$$

$$q_e = B \ln K_T + B \ln C_e.$$

The equations above show that the adsorption constants for all models are  $K_L$ ,  $K_F$ , and  $K_T$ ,  $q_m$  represents the maximum adsorption capacity ( $\text{mg g}^{-1}$ ), and  $n$  represents the linear factor. The Langmuir model describes multilayer adsorption and homogenous and is a good model, while the Freundlich model is monolayer adsorption and is the most

widely used model. Finally, the Temkin model describes adsorption as a strong interference between the surface of the adsorbent material and the absorbed cations [33].

Figure 12 shows the adsorption results for all the models used and the isotherm constants shown in Table 4, where we observe that the adsorption process of the lead ion on the surface of S-CNs applies to the Langmuir model of the value  $R^2=0.993$ . While adsorption does not apply to the Freundlich and Temkin models because the values of the correlation coefficients are slightly. This indicates that adsorption is multilayered.

3.2.5. *Effect of Temperature on Adsorption Process.* Temperature is one of the factors that greatly affect the adsorption capacity. The temperature is studied in the range (20–50)°C. Figure 13 shows that the adsorption capacity increases gradually with increasing temperature to the high adsorption efficiency at 50°C. Observe that the

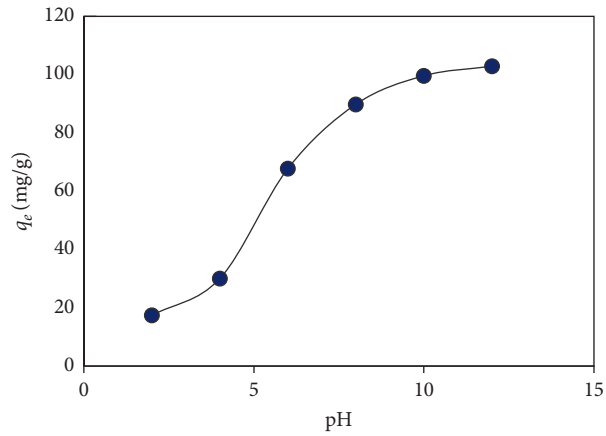


FIGURE 11: Effect of pH solution on adsorption Pb (II) on S-CNs.

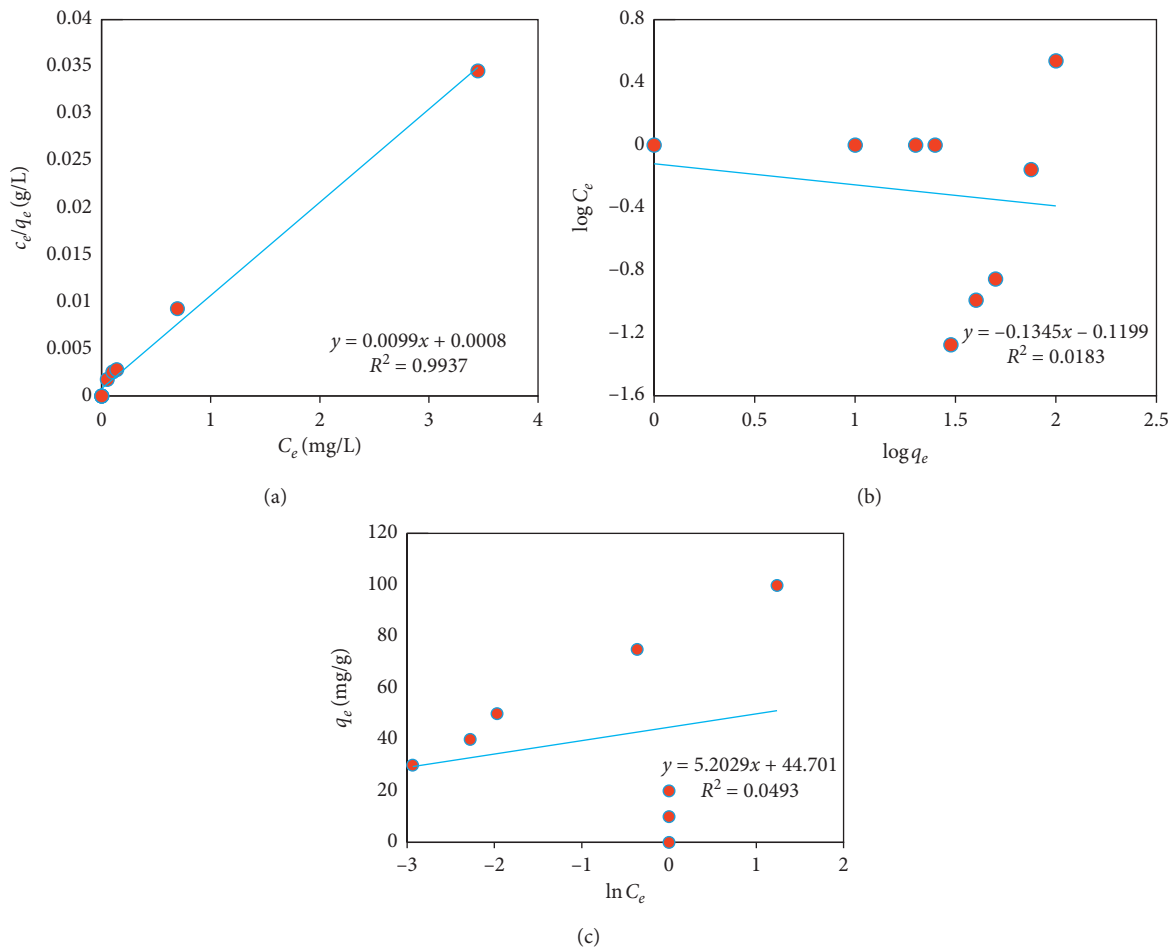


FIGURE 12: Linearized form of (a) Langmuir model, (b) Freundlich model, and (c) Temkin model of lead ion.

TABLE 4: Langmuir, Freundlich, and Temkin isotherm constants for Pb (II) uptaken by S-CNs.

Metal	Langmuir equation			Freundlich equation			Temkin equation		
	$K_L$	$q_m$	$R^2$	$K_F$	$n$	$R^2$	$K_T$	$B$	$R^2$
Pb (II)	0.005	39.566	0.993	35.880	30.950	0.003	69.686	9.850	0.033

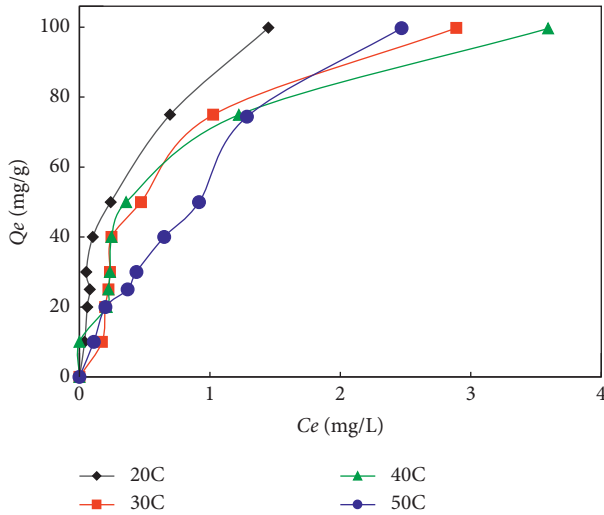


FIGURE 13: Effect of temperature on the adsorption capacity of Pb (II).

TABLE 5: Thermodynamic parameters of adsorption of Pb (II).

Metal	$\Delta H$ (kJ·mol <sup>-1</sup> )	$\Delta G$ (kJ·mol <sup>-1</sup> )	$\Delta S$ (J·mol <sup>-1</sup> ·K <sup>-1</sup> )	Equilibrium constant (K)
Pb (II)	-5.441	-1.633	+37.193	731.200

high temperature increases the solubility of the Pb (II), leads to high adsorption efficiency. Finally, high temperature increases kinetic energy with increased diffusion of cations on the effective sites of the surface of S-CNs [34]. The equations below show the use of thermodynamic parameters to identify the spontaneous reaction and determine the reaction of exothermic or endothermic and random system.

$$\begin{aligned}\Delta G &= -RT \ln K, \\ \Delta G &= \Delta H - T\Delta S, \\ \Delta S &= \frac{\Delta H - \Delta G}{T}, \\ \ln K &= \frac{\Delta S}{R} - \frac{\Delta H}{RT},\end{aligned}\quad (5)$$

where  $\Delta G^\circ$  represents the Gibbs energy,  $\Delta H^\circ$  represents the enthalpy change,  $\Delta S^\circ$  represents the change in entropy,  $T$  is the absolute temperature (K), and  $R$  is the general constant of gases (8.314 J/mol·K). By drawing  $\ln K$  with inverted time ( $T^{-1}$ ), we obtain values ( $\Delta H^\circ$  and  $\Delta S^\circ$ ) from the slope and intercept, respectively. Table 5 shows that the value of the Gibbs energy for each temperature is negative, and this indicates that the adsorption process is spontaneous reaction. Also, the exothermic reaction depends on the negative value  $\Delta H^\circ$ . Finally, the high positive value of the change in entropy takes place in the highly randomized system [35].

**3.2.6. Effect of Ionic Strength.** Ionic intensity is one of the factors influencing on the adsorption process of Pb (II) on

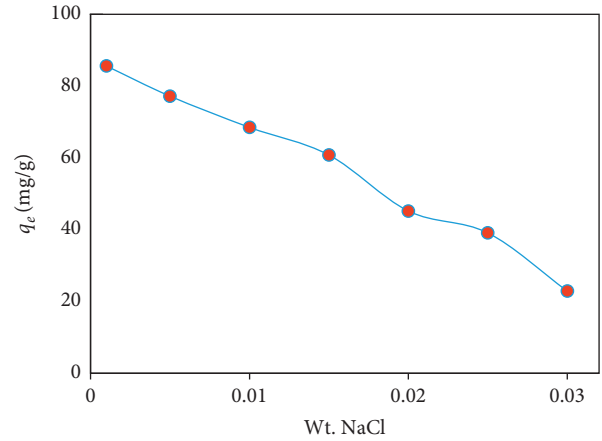


FIGURE 14: Effect of ionic strength on adsorption Pb (II) ions on S-CNs.

the surface of S-CNs. Different weights from salt are used in the range 0.001–0.03 g to know the effect of salt weight on the efficiency of pollutant removal. Figure 14 shows increase in salt weight with the decrease in the adsorption capacity. In previous research, low adsorption capacity with increased salt weight due to the ability of sodium ions to block lead ions for active sites on the surface of S-CNs [36].

## 4. Literature

A list of some previous work prepared of CNs is given in Table 1.

## 5. Conclusions

Carbon nanospheres (CNs) were prepared using a natural extract, and then sodium hydroxide (NaOH) solution and sulfuric acid were added to the preparation of N-CNs and S-CNs, respectively. The extract adds functional groups to the carbon nanosphere surface to increase the adsorption capacity of the Pd (II) from aqueous solution. The resulting CNs showed homogenous nanospheres with an interlayer distance of 4.5 nm, as shown by TEM. The lead ion adsorption process based on the thermodynamic study is spontaneous and exothermic, while kinetic studies show that adsorption process follows both models. It can be expected that the carbon nanospheres (CNs) are additionally appropriate for numerous other uses, for example, drug delivery, sensors, heterogeneous catalysis, and manufacture of functional polymer composites.

## Data Availability

All data are enclosed within the manuscript.

## Conflicts of Interest

The authors declare that they have no conflicts of interest.

## References

- [1] N. Zhao, J. Wang, C. Shi, E. Liu, J. Li, and C. He, "Chemical vapor deposition synthesis of carbon nanospheres over Fe-based glassy alloy particles," *Journal of Alloys and Compounds*, vol. 617, pp. 816–822, 2014.
- [2] A. A. Deshmukh, S. D. Mhlanga, and N. J. Coville, "Carbon spheres," *Materials Science and Engineering: R: Reports*, vol. 70, no. 1–2, pp. 1–28, 2010.
- [3] A. Nieto-Márquez, R. Romero, A. Romero, and J. L. Valverde, "Carbon nanospheres: synthesis, physicochemical properties and applications," *Journal of Materials Chemistry*, vol. 21, no. 6, pp. 1664–1672, 2011.
- [4] J. Choma, D. Jamiola, K. Augustynek, M. Marszewski, M. Gao, and M. Jaroniec, "New opportunities in Stöber synthesis: preparation of microporous and mesoporous carbon spheres," *Journal of Materials Chemistry*, vol. 22, no. 25, pp. 12636–12642, 2012.
- [5] C. X. Guo and C. M. Li, "A self-assembled hierarchical nanostructure comprising carbon spheres and graphene nanosheets for enhanced supercapacitor performance," *Energy & Environmental Science*, vol. 4, no. 11, pp. 4504–4507, 2011.
- [6] J. Shu, R. Ma, M. Shui et al., "Facile controlled growth of silica on carbon spheres and their superior electrochemical properties," *RSC Advances*, vol. 2, no. 13, pp. 5806–5814, 2012.
- [7] J. Shu, R. Ma, M. Shui et al., "Controlled synthesis of ultrathin hollow mesoporous carbon nanospheres for supercapacitor applications," *Industrial & Engineering Chemistry Research*, vol. 53, no. 8, pp. 3125–3130, 2014.
- [8] C. Zhang, G. Bhargava, M. D. Elwell et al., "Hollow graphitic carbon nanospheres: synthesis and properties," *Journal of Materials Science*, vol. 49, no. 5, pp. 1947–1956, 2014.
- [9] X.-Y. Liu, B.-C. Huang, and N. J. Coville, "The Fe (CO) 5 catalyzed pyrolysis of pentane: carbon nanotube and carbon nanoball formation," *Carbon*, vol. 40, no. 15, pp. 2791–2799, 2002.
- [10] H. Hou, A. K. Schaper, F. Weller, and A. Greiner, "Carbon nanotubes and spheres produced by modified ferrocene pyrolysis," *Chemistry of Materials*, vol. 14, no. 9, pp. 3990–3994, 2002.
- [11] Y. Wang, D. Nepal, and K. E. Geckeler, "Hollow porous carbon nanospheres with large surface area and stability, assembled from oxidized fullerenes," *Journal of Materials Chemistry*, vol. 15, no. 10, pp. 1049–1054, 2005.
- [12] Z. Wang, P. Xiao, and N. He, "Synthesis and characteristics of carbon encapsulated magnetic nanoparticles produced by a hydrothermal reaction," *Carbon*, vol. 44, no. 15, pp. 3277–3284, 2006.
- [13] R. Atchudan, T. N. Jebakumar Immanuel Edison, S. Perumal, and Y. R. Lee, "Indian gooseberry-derived tunable fluorescent carbon dots as a promise for in vitro/in vivo multicolor bioimaging and fluorescent ink," *ACS Omega*, vol. 3, no. 12, pp. 17590–17601, 2018.
- [14] N. Koprinarov and M. Konstantinova, "Preparation of carbon spheres by low-temperature pyrolysis of cyclic hydrocarbons," *Journal of Materials Science*, vol. 46, no. 5, pp. 1494–1501, 2011.
- [15] R. Atchudan, T. N. J. I. Edison, K. R. Aseer, S. Perumal, and Y. R. Lee, "Hydrothermal conversion of *Magnolia liliiflora* into nitrogen-doped carbon dots as an effective turn-off fluorescence sensing, multi-colour cell imaging and fluorescent ink," *Colloids and Surfaces B: Biointerfaces*, vol. 169, pp. 321–328, 2018.
- [16] Y. Shin, L.-Q. Wang, I.-T. Bae, B. W. Arey, and G. J. Exarhos, "Hydrothermal syntheses of colloidal carbon spheres from cyclodextrins," *The Journal of Physical Chemistry C*, vol. 112, no. 37, pp. 14236–14240, 2008.
- [17] R. Atchudan, T. N. J. I. Edison, K. R. Aseer, S. Perumal, N. Karthik, and Y. R. Lee, "Highly fluorescent nitrogen-doped carbon dots derived from *Phyllanthus acidus* utilized as a fluorescent probe for label-free selective detection of Fe<sup>3+</sup> ions, live cell imaging and fluorescent ink," *Biosensors and Bioelectronics*, vol. 99, pp. 303–311, 2018.
- [18] A. Demirbas, "Agricultural based activated carbons for the removal of dyes from aqueous solutions: a review," *Journal of Hazardous Materials*, vol. 167, no. 1–3, pp. 1–9, 2009.
- [19] A. El-Menshawly, I. Kenawy, and A. El-Asmy, "Modification of chloromethylated polystyrene with 2-mercaptobenzothiazole for application as a new sorbent for preconcentration and determination of Ag<sup>+</sup> from different matrices," *Journal of Hazardous Materials*, vol. 173, no. 1–3, pp. 523–527, 2010.
- [20] M. Doorley, S. R. Mishra, M. Laradji, R. K. Gupta, and K. Ghosh, "Carbon nanospheres: "green" synthesis, characterization, and growth kinetics," *MRS Online Proceedings Library Archive*, vol. 1054, 2007.
- [21] B. Chang, D. Guan, Y. Tian, Z. Yang, and X. Dong, "Convenient synthesis of porous carbon nanospheres with tunable pore structure and excellent adsorption capacity," *Journal of Hazardous Materials*, vol. 262, pp. 256–264, 2013.
- [22] R. Atchudan, T. N. J. I. Edison, S. Perumal, P. Thirukumaran, R. Vinodh, and Y. R. Lee, "Green synthesis of nitrogen-doped carbon nanograss for supercapacitors," *Journal of the Taiwan Institute of Chemical Engineers*, vol. 102, pp. 475–486, 2019.
- [23] R. Atchudan, T. N. J. I. Edison, S. Perumal, N. Clament Sagaya Selvam, Y. R. Lee, and Y. R. Lee, "Green synthesized multiple fluorescent nitrogen-doped carbon quantum dots as an efficient label-free optical nanoprobe for in vivo live-cell imaging," *Journal of Photochemistry and Photobiology A: Chemistry*, vol. 372, pp. 99–107, 2019.
- [24] S. H. A. Altaa, H. A. H. Alshamsi, and L. S. J. Al-Hayder, "Rhodamine B removal on A-rGO/cobalt oxide nanoparticles composite by adsorption from contaminated water," *Journal of Molecular Structure*, vol. 1161, pp. 356–365, 2017.
- [25] X. Cui, Y. Wang, J. Liu et al., "Dual functional N- and S-doped carbon dots as the sensor for temperature and Fe<sup>3+</sup> ions," *Sensors and Actuators B: Chemical*, vol. 242, pp. 1272–1280, 2017.
- [26] D. Gu, S. Shang, Q. Yu, and J. Shen, "Green synthesis of nitrogen-doped carbon dots from lotus root for Hg (II) ions detection and cell imaging," *Applied Surface Science*, vol. 390, pp. 38–42, 2016.
- [27] J. Jiang, Y. He, S. Li, and H. Cui, "Amino acids as the source for producing carbon nanodots: microwave assisted one-step synthesis, intrinsic photoluminescence property and intense chemiluminescence enhancement," *Chemical Communications*, vol. 48, no. 77, pp. 9634–9636, 2012.
- [28] D. Sun, R. Ban, P.-H. Zhang, G.-H. Wu, J.-R. Zhang, and J.-J. Zhu, "Hair fiber as a precursor for synthesizing of sulfur- and nitrogen-co-doped carbon dots with tunable luminescence properties," *Carbon*, vol. 64, pp. 424–434, 2013.
- [29] R. Atchudan, N. Muthuchamy, T. N. J. I. Edison et al., "An ultrasensitive photoelectrochemical biosensor for glucose based on bio-derived nitrogen-doped carbon sheets wrapped titanium dioxide nanoparticles," *Biosensors and Bioelectronics*, vol. 126, pp. 160–169, 2019.

- [30] D. B. Williams and C. B. Carter, "The transmission electron microscope," *Transmission Electron Microscopy*, pp. 3–22, Springer, New York, NY, USA, 2009.
- [31] X. Song, P. Gunawan, R. Jiang, S. S. J. Leong, K. Wang, and R. Xu, "Surface activated carbon nanospheres for fast adsorption of silver ions from aqueous solutions," *Journal of Hazardous Materials*, vol. 194, pp. 162–168, 2011.
- [32] R. Atchudan, T. N. J. I. Edison, S. Perumal, A. S. Parveen, and Y. R. Lee, "Electrocatalytic and energy storage performance of bio-derived sulphur-nitrogen-doped carbon," *Journal of Electroanalytical Chemistry*, vol. 833, pp. 357–369, 2019.
- [33] Y. Gao, Y. Li, L. Zhang et al., "Adsorption and removal of tetracycline antibiotics from aqueous solution by graphene oxide," *Journal of Colloid and Interface Science*, vol. 368, no. 1, pp. 540–546, 2012.
- [34] P. Banerjee, S. Sau, P. Das, and A. Mukhopadhyay, "Optimization and modelling of synthetic azo dye wastewater treatment using Graphene oxide nanoplatelets: characterization toxicity evaluation and optimization using Artificial Neural Network," *Ecotoxicology and Environmental Safety*, vol. 119, pp. 47–57, 2015.
- [35] H. Wang, X. Yuan, Y. Wu et al., "Adsorption characteristics and behaviors of graphene oxide for Zn (II) removal from aqueous solution," *Applied Surface Science*, vol. 279, pp. 432–440, 2013.
- [36] L. Ji, W. Chen, J. Bi et al., "Adsorption of tetracycline on single-walled and multi-walled carbon nanotubes as affected by aqueous solution chemistry," *Environmental Toxicology and Chemistry*, vol. 29, no. 12, pp. 2713–2719, 2010.
- [37] T. Hu, Y. Li, W. Gao, X. Wang, and Y. Tian, "Engineering of rich nitrogen-doped and magnetic mesoporous carbon nanospheres with predictable size uniformity for acid dye molecules adsorption," *Microporous and Mesoporous Materials*, vol. 279, pp. 234–244, 2019.
- [38] Y. Li, F.-T. Liu, H.-X. Zhang, X. Li, X.-F. Dong, and C.-W. Wang, "DMF-treated strategy of carbon nanospheres for high-efficient and selective removal of organic dyes," *Applied Surface Science*, vol. 484, pp. 144–151, 2019.
- [39] K. Zhu, C. Chen, M. Xu et al., "In situ carbothermal reduction synthesis of Fe nanocrystals embedded into N-doped carbon nanospheres for highly efficient U (VI) adsorption and reduction," *Chemical Engineering Journal*, vol. 331, pp. 395–405, 2018.
- [40] J. Liu, J. Wu, J. Chong, X. Wang, and Z. Zhu, "Hexamine-induced co-assembly to N-doped ferromagnetic mesoporous carbon nanospheres for dye adsorption," *Materials Letters*, vol. 239, pp. 86–89, 2019.